

HD 2685 *b* : A Hot-Jupiter orbiting an early F-type star detected by TESS[★]

Matías I. Jones¹, Rafael Brahm^{2,3}, Nestor Espinoza⁴, Songhu Wang^{5**}, Avi Shporer⁶, Thomas Henning⁴, Andrés Jordán^{2,3}, Paula Sarkis⁴, Leonardo A. Paredes⁷, James Hodari-Sadiki⁷, Todd Henry⁸, Bryndis Cruz⁵, Louise D. Nielsen⁹, François Bouchy⁹, Francesco Pepe⁹, Damien Ségransan⁹, Oliver Turner⁹, Stéphane Udry⁹, Gaspar Bakos¹⁰, David Osip¹¹, Vincent Suc², Carl Ziegler¹², Andrei Tokovinin¹³, Nick M. Law¹⁴, Andrew W. Mann¹⁴, Howard Relles⁶, Karren A. Collins¹⁵, Daniel Bayliss¹⁶, Elyar Sedaghati¹, David W. Latham¹⁵, Sara Seager^{6,17}, Joshua N. Winn¹⁸, Jon M. Jenkins¹⁹, Jeffrey C. Smith^{19,20}, Misty Davies¹⁹, Peter Tenenbaum^{19,20}, Jason Dittmann^{6**}, Andrew Vanderburg^{21***}, Jessie L. Christiansen²², Kari Haworth⁶, John Doty⁶, Gabor Furesz⁶, and Greg Laughlin⁵

¹ European Southern Observatory, Alonso de Córdova 3107, Vitacura, Casilla 19001, Santiago, Chile
e-mail: mjones@eso.org

² Instituto de Astrofísica, Facultad de Física, Pontificia Universidad Católica de Chile, Av. Vicuña Mackenna 4860, 7820436 Macul, Santiago, Chile

³ Millennium Institute of Astrophysics, 7820436 Santiago, Chile

⁴ Max-Planck-Institut für Astronomie, Königstuhl 17, D-69117 Heidelberg, Germany

⁵ Department of Astronomy, Yale University, New Haven, CT 06511, USA

⁶ Department of Physics and Kavli Institute for Astrophysics and Space Research, Massachusetts Institute of Technology, Cambridge, MA 02139, USA

⁷ Physics and Astronomy Department, Georgia State University, Atlanta, GA 30302, USA

⁸ RECONS Institute, Chambersburg, PA, USA

⁹ Geneva Observatory, University of Geneva, Chemin des Maillettes 51, 1290 Versoix, Switzerland

¹⁰ Department of Astrophysical Sciences, Princeton University, NJ 08544, USA

¹¹ Las Campanas Observatory, Carnegie Institution of Washington, Colina el Pino, Casilla 601 La Serena, Chile

¹² Dunlap Institute for Astronomy and Astrophysics, University of Toronto, Ontario M5S 3H4, Canada

¹³ Cerro Tololo Inter-American Observatory, Casilla 603, La Serena, Chile

¹⁴ Department of Physics and Astronomy, University of North Carolina at Chapel Hill, Chapel Hill, NC 27599-3255, USA

¹⁵ Harvard-Smithsonian Center for Astrophysics, 60 Garden Street, Cambridge, MA 02138 USA

¹⁶ Department of Physics, University of Warwick, Gibbet Hill Rd., Coventry, CV4 7AL, UK

¹⁷ Department of Earth and Planetary Sciences, MIT, 77 Massachusetts Avenue, Cambridge, MA 02139, USA

¹⁸ Department of Astrophysical Sciences, Princeton University, 4 Ivy Lane, Princeton, NJ 08544, USA

¹⁹ NASA Ames Research Center, Moffett Field, CA 94035, USA

²⁰ SETI Institute, 189 Bernardo Avenue, Suite 100, Mountain View, CA 94043, USA

²¹ Department of Astronomy, The University of Texas at Austin, Austin, TX 78712, USA

²² IPAC, Mail Code 100-22, Caltech, 1200 E. California Blvd. Pasadena, CA 91125, USA

ABSTRACT

We report on the confirmation of a transiting giant planet around the relatively hot ($T_{\text{eff}} = 6801 \pm 56$ K) star HD 2685, whose transit signal was detected in Sector 1 data of the TESS mission. We confirmed the planetary nature of the transit signal by using Doppler velocimetric measurements with CHIRON, CORALIE and FEROS, as well as photometric data with CHAT and LCOGT. From the photometry and radial velocities joint analysis, we derived the following parameters for HD 2685 *b*: $P=4.12692 \pm 0.00004$ days, $M_p=1.18 \pm 0.09 M_J$ and $R_p=1.44 \pm 0.01 R_J$. This system is a typical example of an inflated transiting Hot-Jupiter in a circular orbit. Given the host star apparent visual magnitude ($V = 9.6$ mag), this is one of the brightest known stars hosting a transiting *Hot-Jupiter*, and a good example of the upcoming systems that will be detected by TESS during the two-year primary mission. This is also an excellent target for future ground and space based atmospheric characterization as well as a good candidate for measuring the projected spin-orbit misalignment angle via the Rossiter-McLaughlin effect.

Key words. Planetary systems – Planets and satellites: gaseous planets – Planet-star interactions

1. Introduction

Transiting planets are of great importance because they provide us with crucial information about their formation and evolution. When transit observations are complemented with precision radial velocity (RV) data, it is possible to accurately determine their mass and radius, and therefore their mean density. Using

* Tables of photometry are available in the electronic version of this paper.

** 51 Pegasi b Fellow

*** NASA Sagan Fellow

this information we can study their internal structure, and compare their parameters with those predicted by theoretical planetary structure models (Baraffe et al. 2014; Thorngren et al. 2016). In addition, due to their proximity to the parent star, we can study how they are affected by the strong stellar irradiation (e.g. Guillot & Showman 2002) and tidal interactions with the host star (Rasio et al. 1996; Matsumura et al. 2010). Moreover, by measuring the stellar obliquity, we can further study different migration scenarios (for a review see Winn & Fabrycky 2015).

During the past decade, the transit method has become the most efficient way to detect compact planetary systems. While it is still challenging to detect transit events from the ground, particularly for sub-mmag transit depths and/or long-duration events, the advent of dedicated space missions has revolutionized the way we study close-in extrasolar planets. In particular, the *Kepler* mission (Borucki et al. 2010) launched in 2009, provided us with thousands of transiting systems¹, including Earth-like, Neptune-sized, and gas giant planets in short-period orbits, also revealing that the majority of the stars in our Galaxy host planets, and in particular the M-dwarfs (Dressing & Charbonneau 2013; Mulders et al. 2015). Unfortunately, most of the candidate systems detected by *Kepler* and its mission extension *K2* are relatively faint, thus their detailed characterization via radial velocity follow-up and transmission spectroscopy is restricted only to the brightest examples.

On the other hand, NASA’s Transiting Exoplanet Survey Satellite (TESS; Ricker et al. 2015), launched in 2018 and already in full operations, will target more than 200,000 stars at 2-minute cadence, 5% of them brighter than ~ 8 mag. Among these bright stars, a total of ~ 100 planets are expected to be detected, with ~ 7 of them orbiting stars with $V \lesssim 6$ mag (Barclay et al. 2018). The recently published inner planet orbiting the naked-eye star π Mensae, detected in TESS’s Sector 1, is a good example of this (Gandolfi et al. 2018; Huang et al. 2018). These newly detected bright transiting systems will be primary targets for further transit studies and detailed atmospheric characterization by ground-based high-resolution transmission spectroscopy and future space missions such as the CHAracterising ExOPlanet Satellite (CHEOPS; Broeg et al. 2013) and the James Web Space Telescope (JWST; Gardner et al. 2006). These systems will also provide us with the opportunity of a dedicated spectroscopic follow-up from the ground, to measure their individual masses (particularly for Earth-sized planets) and to study the host star spin-orbit alignment (obliquity) via the Rossiter-McLaughlin effect (e.g. Queloz et al. 2000).

In this paper we report on the spectroscopic confirmation of a transiting *Hot-Jupiter* around the early F-type star HD 2685 (TIC 267263253, TOI 135), discovered in Sector 1 data of the TESS mission. After HD 202772 A b (Wang et al. 2018b), this is the second *Hot-Jupiter* detected by the TESS mission. With a visual magnitude $V = 9.6$, HD 2685 is also among the brightest known stars that host a *Hot-Jupiter*, making this system an ideal target for a detailed follow-up characterization, and a good example of the upcoming transiting planets that will be detected by TESS.

The paper is structured as follows. In Section 2 we describe the photometric and spectroscopic observations as well as the data analysis. In Section 3 we derive the stellar properties. In Section 4 we present the global modelling using the combined radial velocities and transit photometry. Finally, the discussion is presented in Section 5.

2. Observations and data analysis

2.1. TESS photometric data

HD 2685 (TIC 267263253, TOI 135) was observed in the high-cadence mode (2-minute exposures) in Sector 1 of the TESS space mission. These observations were collected by Camera 3, between July 25 and August 22, 2018. HD 2685 is not planned to be observed in other TESS sectors during the TESS primary mission. The light curve was processed by the Science Processing Operations Center (SPOC) pipeline (Jenkins et al. 2016), which is based on the Kepler Mission science pipeline (Jenkins 2017) and made available by the NASA Ames SPOC center and at the MAST archive². This dataset is comprised of a total of 18097 individual measurements, in which a total of 7 transit events were identified, with depths of $\sim 10,000$ ppm and duration of ~ 4.5 hours. After masking out the transits, we detrended the light curve using a gaussian process modelling, with the quasi-periodic kernel presented in (Foreman-Mackey et al. 2017). Figure 1 shows the detrended and phase-folded TESS light curve of HD 2685. The blue line corresponds to the best-fitting model described in section 4.

2.2. CHAT photometry

In addition to the TESS photometric data, we also collected a total of 411 ground-based measurements using the Chilean-Hungarian Automated Telescope (CHAT; Jordán et al. 2018, in prep.), installed at Las Campanas Observatory, in Chile. Observations were acquired on September 22 UT of 2018 using the *i'* sloan filter. The exposure time per image was of 14 s, which translated in a cadence of ≈ 25 s. A mild defocus was applied. The data were reduced through a dedicated automatic pipeline (Hartman et al. 2018; Jordán et al. 2018). Thanks to the spatial resolution of CHAT (pixel scale of 0.6 arcsec), these were the first observations that helped us to confirm the source of the transit signal, discarding other potential sources in the TESS field of view. Figure 1 shows the CHAT photometry of HD 2685 during the transit. The residual scatter is 3105 ppm and 1001 ppm when binned to 5 minutes bins. As can be seen, even though the CHAT data only covered the second half of one transit event, the observed transit depth is consistent with the TESS data.

2.3. Las Cumbres Observatory photometry

We performed ground-based photometric follow-up using the Las Cumbres Observatory Global Telescope (LCOGT³) network (Brown et al. 2013). On 2018 September 22 UT, we observed an almost complete transit (missing the egress) in the *i*-band using the LCOGT 0.4-m telescopes situated at South Africa Astronomical Observatory (SAAO) at Sutherland, South Africa. This observations were taken the same night as the CHAT observations, meaning that we covered one full transit using two different instruments. The observations were done with the SBIG camera and consisted of 394 exposures with an exposure time of 30s, taken while the telescope was defocused by 1.5mm to spread the stellar point-spread function over more pixels, thereby reducing the impact of flat-fielding uncertainties. The data was reduced by the LCOGT pipeline and photometry was carried out with AstroImageJ (Collins et al. 2017). The light curve is plotted in Fig. 1. The residual scatter is 2560 ppm per point and 786 ppm when binned to 5 minutes bins. These observations were made

¹ <https://keplerscience.arc.nasa.gov/>

² <https://archive.stsci.edu/>

³ <http://lco.gobal>

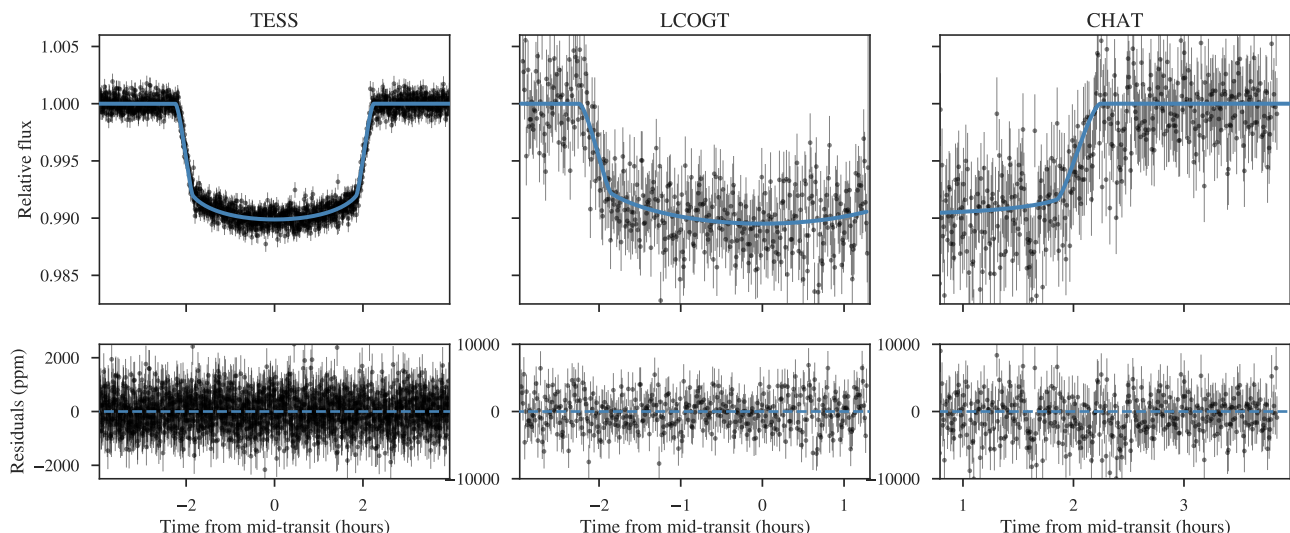


Fig. 1. *Left:* Detrended and phase-folded TESS light curve of HD 2685 during the transit. The solid blue line corresponds to the transit fit from the joint analysis. *Middle:* LCOGT photometric data covering the ingress and mid part of one individual transit. *Right* CHAT data covering the egress of the same transit event observed by LCOGT.

as part of an LCOGT Key Project to follow-up TESS transiting planet candidates and characterize transiting planets using the LCOGT network⁴.

2.4. Speckle imaging

The relatively large 21'' pixels of TESS can result in photometric contamination from nearby sources. These must be accounted for to rule out astrophysical false positives, such as background eclipsing binaries, and to correct the estimated planetary radius, initially derived from the diluted transit in a blended light curve. We searched for close companions to HD 2685 with speckle imaging on the 4.1-m Southern Astrophysical Research (SOAR) telescope (Tokovinin 2018) on 2018 September 25 UT. The 5σ detection sensitivity and auto-correlation function of the observation are shown in Figure 2. We detected no nearby stars down to a magnitude difference of 4 within 0.2'' and 5 magnitudes within 1'' of HD 2685 in the SOAR images.

2.5. CHIRON Radial Velocities

As part of a two-week spectroscopic confirmation campaign of a handful of short-period transiting candidate planets detected by TESS, we obtained a total of 11 spectra of HD 2685 using CHIRON (Tokovinin et al. 2013), a fibre-fed high-resolution spectrograph, mounted on the SMARTS 1.5m telescope, at the Cerro Tololo Inter-American Observatory, in Chile. The spectra were taken using a 2.7 arcsec diameter fibre on sky, with the high efficient image slicer mode. The exposure time was 1200 seconds, leading to a mean signal-to-noise-ratio (SNR) per pixel at 5500 Å of ~ 45 . From the spectra, we computed relative RV measurements using the cross-correlation technique, and correcting the night drift using Th-Ar spectra taken before and after each science exposure, as explained in Wang et al. (2018b). This method is applied individually to a total of 41 orders covering the wavelength range between $\sim 4500 - 7000$ Å. The mean RV uncertainty per epoch is $\sim 30 \text{ m s}^{-1}$, explained mainly due to

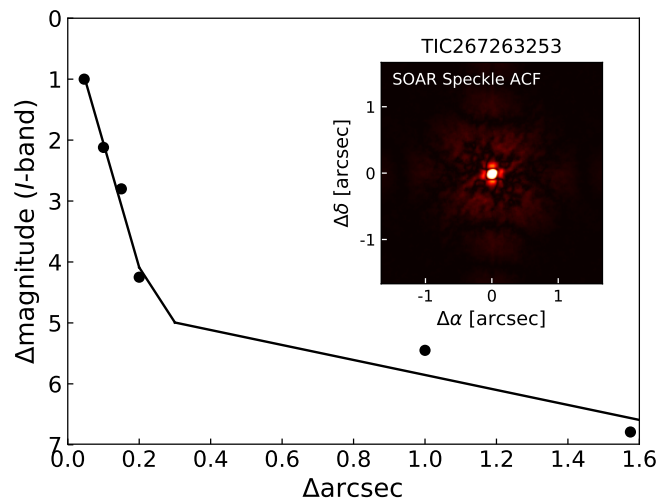


Fig. 2. Speckle auto-correlation function obtained in the *I*-band, at the SOAR telescope. The black dots correspond to the $5\text{-}\sigma$ contrast curve for HD 2685. The solid line corresponds to the linear fit of the data, at separations smaller and larger than ~ 0.2 arcsec.

the fast stellar rotation. The resulting RVs are plotted in Figure 3 and are also listed in Table 1. The resulting CHIRON RVs of HD 2685 revealed an amplitude of $\geq 100 \text{ m s}^{-1}$, in phase with the orbital period detected in the TESS photometry. Additionally, from the cross-correlation-function (CCF) we computed the bisector velocity span (BVS), which are also listed in Table 1. Figure 4 shows the BVS versus the RVs. While the BVS scatter is large, they do not show a correlation with the RVs. In fact, the Pearson correlation coefficient between the CHIRON BVS and RVs is -0.14 .

2.6. FEROS Radial Velocities

The CHIRON data were complemented with the Fiber-fed Extended Range Optical Spectrograph (FEROS; Kaufer et al. 1999)

⁴ space.mit.edu/~shporer/LCOKP

spectra, using the simultaneous calibration technique (Baranne et al. 1996). In this mode, the 2.0'' diameter science fibre is illuminated by the star, while the second fibre is illuminated by a Th-Ar reference lamp, which is used to correct for the RV drift. We obtained five spectra of HD 2685 with an exposure time of 300 seconds, leading to a mean SNR per resolution element of ≈ 100 . The data reduction and RV calculation were performed with the CERES pipeline (Brahm et al. 2017a). The reduction process is relatively standard for echelle spectra, and consists of a bias correction, flat field order tracing and optimal extraction. This method is applied to a total of 25 orders covering the wavelength region between ~ 3900 – 6800\AA . Finally, each order is wavelength calibrated. The wavelength solution is accurate at the $\sim 2\text{ m s}^{-1}$ level, and is obtained from a total ~ 1000 Th-Ar emission lines. The RVs are computed via cross-correlation between each individual order with a binary numerical mask, and are corrected for the night drift using the Th-Ar spectra. The resulting velocities are plotted in Figure 3, and are listed in Table 1. Similarly we computed FEROS BVS values, which are also listed in Table 1, and plotted in Figure 4. As can be seen there is no obvious correlation between these two quantities. The Pearson correlation coefficient between the FEROS BVS and the corresponding RVs is 0.24.

2.7. CORALIE Radial Velocities

Additional 14 spectra were obtained with the CORALIE high resolution spectrograph on the Swiss 1.2 m Euler telescope at La Silla Observatories, Chile (Queloz et al. 2001), between 21 September and 28 October 2018. CORALIE is fed by a 2'' science fibre and a secondary fibre with simultaneous Fabry-Perot for wavelength calibration. RVs were computed by cross-correlation with a binary G2 mask. Our exposures varied between 900 and 1800 seconds depending on the weather conditions. We obtain a final accuracy of 30–40 m/s which is limited by the stellar rotation due to broadening of the CCF. The resulting velocities are plotted in Figure 3, and are listed in Table 1. Additionally, we computed the BVS values at each observing epoch, which are also listed in Table 1 and plotted in Figure 3. The Pearson linear coefficient between the CORALIE RVs and BVS values is 0.01.

3. Host stars properties.

We first used the co-added FEROS spectra to estimate the atmospheric parameters (T_{eff} , $\log g$, $[\text{Fe}/\text{H}]$) and the projected rotational velocity ($v \sin i$) of HD 2685. Specifically, we use the ZASPE code (Brahm et al. 2017b) to compare the observed spectra to a grid of synthetic models generated from the ATLAS9 model atmospheres (Castelli & Kurucz 2004). The comparison is performed in an iterative fashion, only in the spectral regions that are more sensitive to changes in the atmospheric parameters. These regions are computed automatically from the gradient of the synthetic grid with respect to the atmospheric parameters. Reliable uncertainties and correlations between the parameters are obtained through Monte Carlo simulations that take into account systematic mismatches between the optimal model and the observed spectrum. Then, we computed the stellar physical parameters, following Brahm et al. (2018). This is done by combining the public broad band photometry, the *Gaia* DR2 parallaxes (*Gaia* collaboration et al. 2018), the derived atmospheric parameters, and the Yonsei-Yale isochrones (Yi et al. 2001). For this, we use the *Gaia* parallax and a BT-Settl-CIFIST spec-

tral energy distribution model having parameters equal to those derived through our spectroscopic analysis to generate synthetic magnitudes. The set of synthetic magnitudes depend on the stellar radius (R_{\star}) and the extinction coefficient (A_V). We then search for the distribution of R_{\star} and A_V by comparing the synthetic magnitudes to the observed ones presented in Table 2. The exploration of the parameter space is performed with the emcee package (Foreman-Mackey et al. 2013). We found that HD 2685 is not significantly affected by interstellar reddening. Finally, to obtain the mass, age and luminosity of the star, we compared its derived effective temperature and radius to that predicted by the Yonsei-Yale isochrones for different masses and evolutionary stages, by fixing the metallicity of the isochrones to the value obtained in the spectroscopic analysis. Again, the parameter space was explored using the emcee package. This procedure, through the estimation of the stellar mass and radius, allows us to estimate a more precise value of $\log g$ than the one obtained with the spectroscopic analysis. Therefore, we performed a new ZASPE run fixing $\log g$ to the value obtained from R_{\star} and M_{\star} , and then we also repeated the determination of these physical parameters. Using this method we obtained the following atmospheric parameters for HD 2685: $T_{\text{eff}} = 6801 \pm 56$, $\log g = 4.22 \pm 0.01\text{ cm s}^{-2}$, $[\text{Fe}/\text{H}] = +0.02 \pm 0.03\text{ dex}$ and $v \sin i = 15.4 \pm 0.2\text{ km s}^{-1}$. Similarly, we obtained the following physical parameters for HD 2685: $M_{\star} = 1.44 \pm 0.02 M_{\odot}$, $R_{\star} = 1.57 \pm 0.01 R_{\odot}$, $L_{\star} = 4.70^{+0.18}_{-0.15} L_{\odot}$ and Age = $1.30 \pm 0.14\text{ Gyr}$. These values are also listed in Table 2, and are those adopted for the rest of the paper.

For comparison, we also derived the stellar atmospheric parameters following the method presented in Jones et al. (2011) and Wang et al. (2018b). Briefly, we used ARES v2 (Sousa et al. 2015) to measure the equivalent width (EW) of ~ 150 Fe I and Fe II absorption lines, from the co-added CHIRON template. These resulting EWs are then compared to the synthetic EWs generated by the MOOG code (Snedden 1973), that solves the radiative transfer equations under the assumptions of local thermodynamic equilibrium, using the Kurucz (1993) stellar atmosphere models. From this analysis we obtained the following atmospheric parameters for HD 2685: $T_{\text{eff}} = 6800 \pm 70\text{ K}$, $\log g = 4.15 \pm 0.15$ and $[\text{Fe}/\text{H}] = -0.08 \pm 0.10$, which are in good agreement with those derived by ZASPE.

Finally, we also performed an analysis of the broadband spectral energy distribution (SED) of HD 2685 together with the *Gaia* DR2 parallax in order to determine an empirical measurement of the stellar radius, following Stassun et al. (2018). For this, we use the $B_T V_T$ magnitudes from *Tycho-2*, the Strömgren *ubvy* magnitudes from Paunzen (2015), the *BVgri* magnitudes from APASS, the *JHK_S* magnitudes from 2MASS, the W1–W4 magnitudes from *WISE*, and the *G* magnitude from *Gaia*. We performed a fit using Kurucz stellar atmosphere models, with the free parameters being the effective temperature, the surface gravity, the metallicity and the extinction, which we restricted to the maximum line-of-sight value from the dust maps of Schlegel et al. (1998). The best fit parameters are $T_{\text{eff}} = 6800 \pm 100\text{ K}$, $\log g = 4.0 \pm 0.25$, $[\text{Fe}/\text{H}] = 0.00 \pm 0.25$, and $A_V = 0.09 \pm 0.02$. These values are consistent with those determined from the spectroscopic analysis. Finally, by taking the stellar bolometric flux computed from the unreddened model SED, and T_{eff} together with the *Gaia* DR2 parallax, gives a stellar radius of $R = 1.57 \pm 0.03 R_{\odot}$, in excellent agreement with that determined from the ZASPE code.

Table 1. Relative radial velocities of HD 2685

BJD -2400000	RV m s ⁻¹	σ_{RV} m s ⁻¹	BVS km s ⁻¹	σ_{BVS} km s ⁻¹	Instrument
58369.6043	186.0	30.8	0.1851	0.1446	CHIRON
58369.8027	89.0	26.0	-0.1046	0.1149	CHIRON
58370.6479	143.7	28.4	0.3017	0.1231	CHIRON
58371.6716	-68.0	36.6	0.3703	0.1771	CHIRON
58371.8098	-26.6	29.5	-0.0291	0.1627	CHIRON
58372.7658	-61.8	24.4	0.0857	0.1114	CHIRON
58373.7375	82.9	45.8	0.1388	0.1910	CHIRON
58375.6807	-51.9	35.9	0.3874	0.1831	CHIRON
58379.7618	-106.6	118.4	0.3702	0.2271	CHIRON
58380.8013	-94.7	32.2	0.0617	0.1077	CHIRON
58384.7577	-92.1	27.0	0.0977	0.1233	CHIRON
58378.8372	2292.0	33.5	-0.0310	0.0300	FEROS
58380.8811	2091.9	36.0	-0.1250	0.0320	FEROS
58382.6972	2306.1	34.8	-0.0770	0.0310	FEROS
58384.7130	2052.5	31.6	-0.0510	0.0280	FEROS
58385.7289	2165.5	30.2	-0.0090	0.0280	FEROS
58382.6797	2178.9	53.2	-0.1756	0.0532	CORALIE
58384.7383	1888.4	49.8	-0.2310	0.0497	CORALIE
58390.6914	2121.9	95.2	-0.8211	0.0952	CORALIE
58397.6797	2062.9	33.2	-0.2030	0.0331	CORALIE
58398.6797	2138.6	41.3	-0.2055	0.0412	CORALIE
58401.7109	1974.4	29.6	-0.0919	0.0295	CORALIE
58404.6992	1984.9	43.9	-0.4070	0.0439	CORALIE
58406.6328	2049.2	53.8	-0.2191	0.0538	CORALIE
58407.5273	2151.5	72.5	0.0080	0.0724	CORALIE
58408.7462	1971.8	35.1	-0.2345	0.0351	CORALIE
58409.6563	1938.5	30.8	-0.2504	0.0307	CORALIE
58410.6250	2154.2	37.3	-0.2356	0.0372	CORALIE
58411.6055	2098.9	40.0	-0.1233	0.0400	CORALIE
58419.6172	2203.5	26.4	-0.2266	0.0263	CORALIE

Table 2. Stellar parameters.

Parameter	HD 2685	Method/Source
T_{eff} (K)	6801 ± 56	ZASPE
$\log g$ (cm s ⁻²)	4.22 ± 0.01	ZASPE + Gaia
[Fe/H] (dex)	$+0.02 \pm 0.03$	ZASPE
$v \sin i$ (km s ⁻¹)	15.4 ± 0.2	ZASPE
M_{\star} (M_{\odot})	1.44 ± 0.02	ZASPE + Gaia + YY
R_{\star} (R_{\odot})	1.57 ± 0.01	ZASPE + Gaia
Distance (pc)	$197.98^{+0.85}_{-0.70}$	Gaia
L_{\star} (L_{\odot})	$4.70^{+0.18}_{-0.15}$	ZASPE + Gaia + YY
Age (Gyr)	1.3 ± 0.1	ZASPE + Gaia + YY
B (mag)	10.05 ± 0.03	Tycho-2
V (mag)	9.59 ± 0.02	Tycho-2
G (mag)	9.5203 ± 0.0003	Gaia
J (mag)	8.825 ± 0.026	2MASS
H (mag)	8.651 ± 0.051	2MASS
K (mag)	8.595 ± 0.019	2MASS

4. Global analysis

We performed a global analysis using both the photometric and spectroscopic data available. To do this, we used the EXOplanet traNsits and rAdIaL veLocity fittER (EXONAILER) which is described in details in Espinoza et al. (2016), and available at

GitHub.⁵ Briefly, we model the detrended light curve using the BATMAN code (Kreidberg 2015), fitting simultaneously the limb-darkening coefficients with the rest of the transit parameters, and following the quadratic limb-darkening law presented in Espinoza & Jordán (2016). Similarly, the RV measurements were modelled using the RAD-VEL package (Fulton et al. 2018). For the RVs, we included a jitter and RV offset as a free-parameter for each RV dataset. We first performed the fit with the eccentricity as a free parameter. We obtained a value of $e = 0.035^{+0.080}_{-0.010}$, which is consistent with a circular orbit. Therefore, we repeated the analysis adopting a zero eccentricity. Table 3 lists the resulting transit values and the derived planetary parameters. Finally, from the derived stellar and planetary parameters we computed the equilibrium temperature (T_{eq}) for HD 2685 *b*. By adopting a zero albedo and assuming a tidally locked planet with no heat distribution ($\beta = 0.5$; Kaltenegger & Sasselov 2011) we obtained $T_{eq} = 2061 \pm 21$ K, for HD 2685 *b*.

4.1. Searching for secondary eclipse and orbital variations

We have examined the phase folded light curve for any variability outside of the transit, including orbital phase curves (Shporer 2017) and secondary eclipse. We did not detect any sinusoidal variation along the orbital phase, which is expected given the system parameters and the sensitivity of the data. We attempted

⁵ <https://github.com/nespinoza/exonailer>

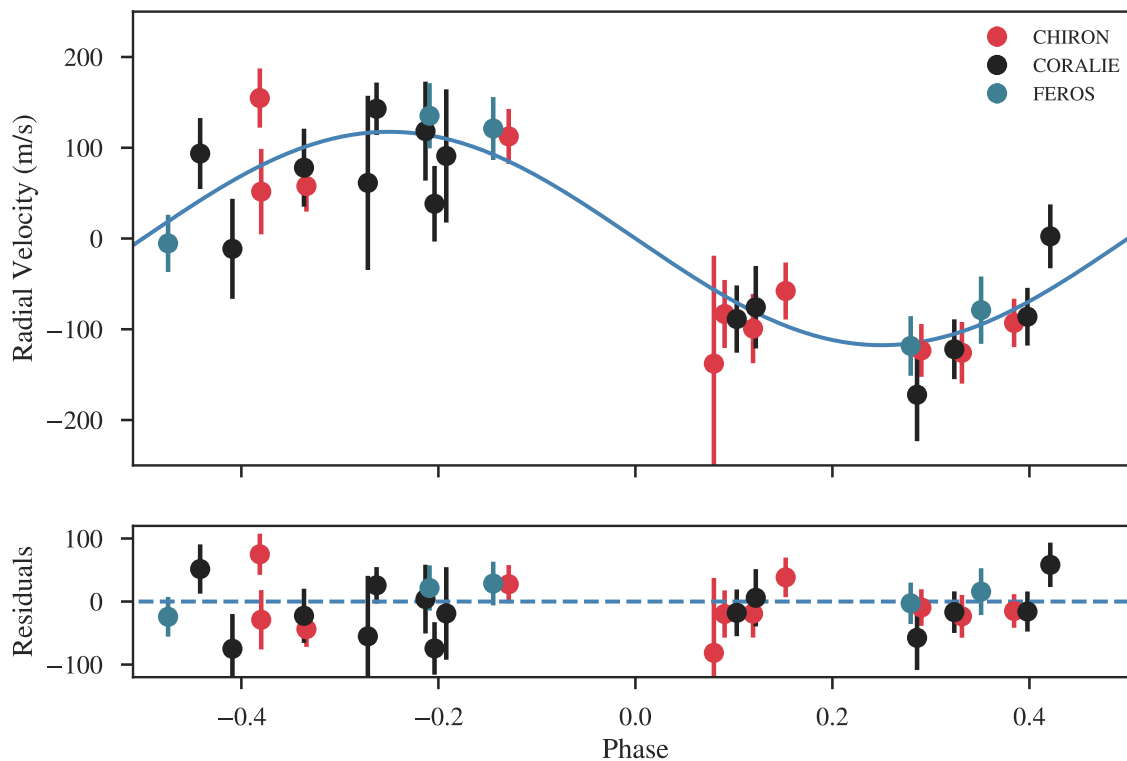


Fig. 3. Phase-folded RV curve of HD 2685. The black, red and blue points correspond to CORALIE, CHIRON and FEROS velocities, respectively. The best keplerian fit from the joint analysis is overplotted. The post-fit residuals are shown in the lower panel.

to measure the secondary eclipse, assuming its duration is identical to that of the transit and taking place exactly half an orbital period away from it. We measured a depth of 17 ± 23 ppm, meaning we do not detect the secondary eclipse and are able to place a 3σ upper limit of 69 ppm on its depth (or a 2σ upper limit of 46 ppm). This translates to a 3σ upper limit on the geometric albedo in the TESS band of $A_g < 0.47$ (or a 2σ upper limit of 0.31). Such an upper limit is consistent with the low geometric albedos found for hot Jupiter exoplanets in visible light (e.g., Heng & Demory 2013; Shporer et al. 2014; Esteves et al. 2015; Angerhausen et al. 2015). In the above we have assumed that the thermal emission has a small to negligible contribution to the secondary eclipse, which in this system reaches only 12 ppm in the extreme case of no heat circulation between the day to night planet hemispheres.

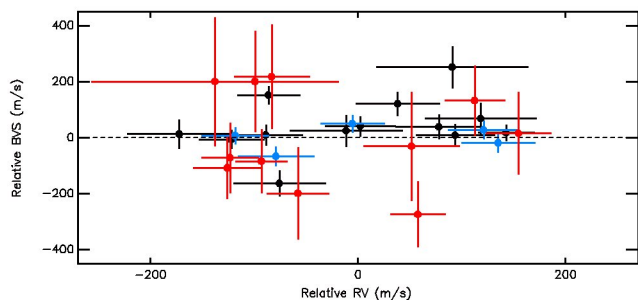


Fig. 4. Bisector velocity span as functions of the CORALIE (black dots), CHIRON (red dots) and FEROS (blue dots) radial velocities. An arbitrary offset is applied to the BVS values.

5. Discussion

In this paper we have presented the radial velocity confirmation of HD 2685 *b*, a transiting *Hot-Jupiter* observed in Sector 1 of the TESS mission. We obtained CHIRON, CORALIE and FEROS spectroscopic data, from which we confirmed the planetary nature of the transit signal detected by TESS. In addition, we obtained CHAT and LCOGT photometric data during one transit event. From the joint analysis we derived the following parameters for HD 2685 *b*: $P = 4.12692 \pm 0.00004$ days, $M_p = 1.18 \pm 0.09 M_J$ and $R_p = 1.44 \pm 0.01 R_J$. We also measured a very low eccentricity ($e = 0.035^{+0.08}_{-0.01}$), which is consistent with a circular orbit.

Figure 5 shows the planetary radius versus mass for known transiting gas giants. The red dot corresponds to HD 2685 *b*. Different iso-density contours are over-plotted (dashed grey lines). Also for comparison, the solid lines mark theoretical models from Baraffe et al. (2014), for no solid core and $100 M_\oplus$ core planets. Similarly, Figure 6 shows the planetary radius versus the planet’s equilibrium Temperature. It can be clearly seen from these two plots that HD 2685 *b* is an inflated *Hot-Jupiter*, whose large radius cannot be explained by current theoretical models of planetary internal structure (e.g. Baraffe et al. 2014) while it is likely explained by the large irradiation received by the parent star (e.g. Hartman et al. 2011; Weiss et al. 2013).

Figure 7 shows the position of HD 2685 in the stellar $\log(g)$ versus T_{eff} parameter space for transiting planets host stars. It can be seen that HD 2685 is among the hottest stars with a known transiting gas giant planet, with only about a dozen host stars at a similar temperature or hotter.

Table 3. Parameters obtained from the global modeling.

Parameter	Value
Light-curve parameters	
P (days)	$4.12692^{+0.00004}_{-0.00004}$
T_c (BJD)	$2458325.78290^{+0.00017}_{-0.00015}$
a/R_\star	$7.6996^{+0.0278}_{-0.0336}$
R_P / R_\star	$0.09481^{+0.00028}_{-0.00026}$
i (deg)	$89.400^{+0.322}_{-0.334}$
q_1 (LCO)	$0.161^{+0.117}_{-0.056}$
q_2 (LCO)	$0.585^{+0.258}_{-0.279}$
q_1 (CHAT)	$0.071^{+0.126}_{-0.051}$
q_2 (CHAT)	$0.286^{+0.345}_{-0.209}$
q_1 (TESS)	$0.146^{+0.039}_{-0.031}$
q_2 (TESS)	$0.389^{+0.098}_{-0.089}$
RV parameters	
e	0 (fixed)
K (m s^{-1})	$117.6^{+9.9}_{-8.7}$
γ_{chiron} (km s^{-1})	0.031 ± 0.012
γ_{feros} (km s^{-1})	2.170 ± 0.016
γ_{coralie} (km s^{-1})	2.061 ± 0.013
σ_{chiron} (m s^{-1})	11^{+13}_{-8}
σ_{feros} (m s^{-1})	9^{+13}_{-7}
σ_{coralie} (m s^{-1})	12^{+18}_{-9}
Planetary parameters	
M_P (M_J)	1.18 ± 0.09
R_P (R_J)	1.44 ± 0.01
a (AU)	$0.0568^{+0.0003}_{-0.0002}$
T_{eq} (K)	2061 ± 21

5.1. Follow-up prospects

HD 2685 has a visual magnitude of $V = 9.6$ mag, meaning it is among the brightest stars with a transiting giant planets, making it a valuable target for detailed follow-up characterization.

Apart from its high apparent brightness ($V = 9.6$ mag), HD 2685 is a relatively hot ($T_{\text{eff}} = 6801 \pm 56$ K) and fast rotating star ($v \sin i = 15.4 \pm 0.2$ km s^{-1}), making this object an excellent target for studying the projected spin-orbit angle via the Rossiter-McLaughlin effect. Knowing the stellar obliquity in transiting giant planets can give us important information about different planetary migration processes. While some of these mechanism predict a damping in the spin-orbit primordial misalignment, if any (Cresswell et al. 2007), some others are expected to alter the mutual inclination angle (e.g. Fabrycky & Tremaine 2007). For this reason, knowing the obliquity angle can help us to distinguish between different migrations scenarios (Wang et al. 2018a). Moreover, Winn et al. (2010) showed that hotter stars ($T_{\text{eff}} \geq 6250$ K) hosting *Hot-Jupiters* have larger obliquity compared to cooler stars. Based on this result, HD 2685 *b* might be expected to be in a high obliquity orbit. From the derived stellar and planet parameters, we predict

an RV semi-amplitude during the transit of ≈ 92 m s^{-1} (assuming an aligned orbit), which can be easily detected given the RV precision attained for this object. Thus this target provides us with an excellent opportunity to further study this observational trend in the high T_{eff} regime (see Addison et al. 2018 for an updated version of this correlation).

On the other hand, transiting exoplanets around bright stars provide a great laboratory for probing physical properties of these alien worlds. Arguably, the most intriguing and accessible of those characteristics is their atmospheric make-up. Studying exoplanetary atmospheres gives us clues about the formation and evolution history of the planetary system, the composition of the initial protoplanetary disk in which the planet was formed, the location of that formation (Madhusudhan et al. 2014; Mordasini et al. 2016), as well as the internal structure of the planet (Dorn et al. 2015). There are a variety of techniques through which minute signatures of exoplanetary atmospheres are detected. The most effective of these has been the transmission spectroscopy that searches for atmospheric imprints on the traversing stellar light (Seager & Sasselov 2000). This is mainly done through either performing mid-to-low resolution, highly time-resolved spectroscopy using multi-object spectrographs from the ground (e.g. FORS2; Bean et al. 2011, Sedaghati et al. 2017, IMACS; Jordán et al. 2013, Espinoza et al. 2018) or space (e.g. HST and Spitzer; Sing et al. 2016), or high resolution stable spectroscopy (e.g. HARPS; Allart et al. 2017). The significance of the detection of various atomic and/or molecular species heavily relies on the brightness of the host star, and the scale height of the exo-atmosphere being probed. Consequently, HD 2685 *b* is an ideal candidate for atmospheric follow-up studies on both accounts. The 9.6 visual magnitude of the host star allows for obtaining high SNR spectra with relatively short exposure times, essential for performing transmission spectroscopy. Additionally, assuming a H/He-dominated atmosphere, the extended scale height of the atmosphere ($H = \frac{k_B T_{\text{eq}}}{\mu m g} \approx 454$ km) due to the large equilibrium temperature expected, leads to significant atmospheric signals, well within the reach of current and future instrumentation (e.g. ESPRESSO, JWST).

Acknowledgements. S.W. and J.S.W. thank the Heising-Simons Foundation for their generous support. CZ is supported by a Dunlap Fellowship at the Dunlap Institute for Astronomy & Astrophysics, funded through an endowment established by the Dunlap family and the University of Toronto. AV's work was performed under contract with the California Institute of Technology (Caltech)/Jet Propulsion Laboratory (JPL) funded by NASA through the Sagan Fellowship Program executed by the NASA Exoplanet Science Institute. A.J. acknowledges support from FONDECYT project 1171208, CONICYT project Basal AFB-170002, and by the Ministry for the Economy, Development, and Tourism's Programa Iniciativa Científica Milenio through grant IC 120009, awarded to the Millennium Institute of Astrophysics (MAS). We acknowledge the use of TESS Alert data, which is currently in a beta test phase, from pipelines at the TESS Science Office and at the TESS Science Processing Operations Center. This research has made use of the Exoplanet Follow-up Observation Program website, which is operated by the California Institute of Technology, under contract with the National Aeronautics and Space Administration under the Exoplanet Exploration Program. This paper includes data collected by the TESS mission, which are publicly available from the Mikulski Archive for Space Telescopes (MAST). This work makes use of observations from the LCOGT network.

References

- Addison, B. C., Wang, S., Johnson, M. C., et al. 2018, *AJ*, 156, 197
 Akeson, R. L., Chen, X., Ciardi, D., et al. 2013, *PASP*, 125, 989
 Allart, R., Lovis, C., Pino, L., et al. 2017, *A&A*, 606, 144
 Angerhausen, D., DeLarme, E., & Morse, J. A. 2015, *PASP*, 127, 1113
 Baraffe, I., Chabrier, G., Fortney, J., & Sotin, C. 2014, *Protostars and Planets VI*, 763
 Baranne, A., Queloz, D., Mayor, M. et al. 1996, *A&A*, 119, 373

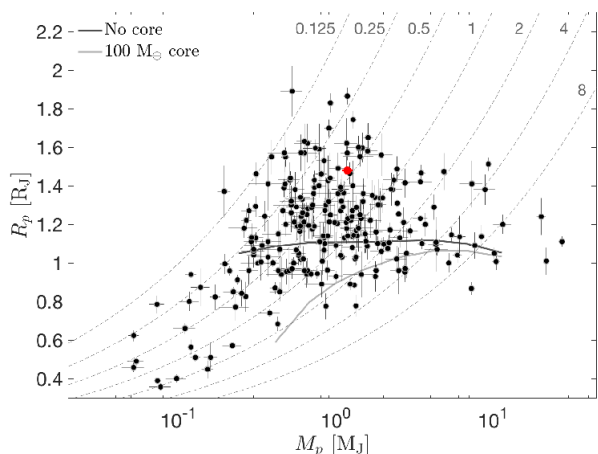


Fig. 5. Planet radius-mass diagram for transiting gas giant planets. The mass axis is plotted in logarithmic scale. The solid lines mark theoretical models taken from Baraffe et al. (2014) for no solid core (black) and a massive core of $100 M_{\text{Earth}}$ (gray). The dashed lines mark isodensity contours, with the density values labeled at the top-right in g cm^{-3} . The position of HD 2685 *b* shows it is an inflated gas giant planet, like other planets of similar mass. The plot includes planets whose radius uncertainty is smaller than $0.15 R_J$ and whose mass uncertainty is smaller than a quarter of the measured mass. Data presented in this plot were obtained from the NASA Exoplanet Archive (Akeson et al. 2013) on October 29, 2018.

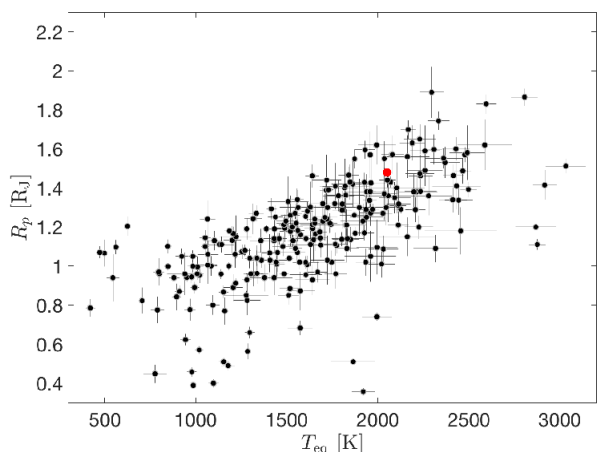


Fig. 6. Planet radius versus equilibrium temperature, showing the well known correlation between the two parameters. The position of HD 2685 *b*, marked in red, is in good agreement with this correlation. The plot includes planets whose radius uncertainty is smaller than $0.15 R_J$ and whose mass uncertainty is smaller than a quarter of the measured mass. Data presented in this plot were obtained from the NASA Exoplanet Archive (Akeson et al. 2013) on October 29, 2018.

Barclay, T., Pepper, J. & Quintana, E. 2018, ArXiv e-prints, arXiv:1804.05050
 Bean, J. L., Désert, J.-M., Kabath, P., et al. 2011, ApJ, 732, 92
 Benneke B. & Seager S., 2012, ApJ, 753, 100
 Borucki, W. J., Koch, D., Basri, G., et al. 2010, Science, 327, 977
 Brahm, R., Jordán, A. & Espinoza, N. 2017a, PASP, 129, 34002
 Brahm R., Jordán A., Hartman J. & Bakos G. 2017b, MNRAS, 467, 971
 Brahm, R., Espinoza, N., Jordán, A. et al. 2018, MNRAS 477, 2572
 Broeg, C., Fortier, A., Ehrenreich, D., et al. 2013, European Physical Journal Web of Conferences 47, 03005
 Brown, T. M., Baliber, N., Bianco, F. B., et al. 2013, PASP, 125, 1031
 Castelli, F., & Kurucz, R. L. 2004, arXiv:0405087
 Collins, K. A., Kielkopf, J. F., Stassun, K. G., & Hessman, F. V. 2017, AJ, 153, 77

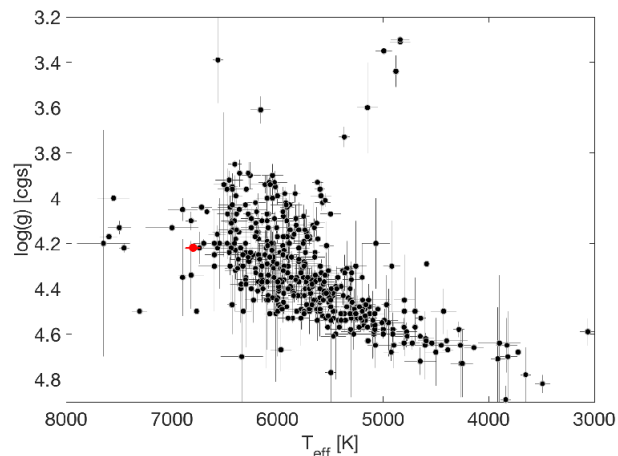


Fig. 7. Stellar surface gravity (in cgs units) versus effective temperature of all known transiting planet host stars where the planet’s mass and radius are both measured. The red dot shows the position of HD 2685. Data presented in this plot were obtained from the NASA Exoplanet Archive (Akeson et al. 2013) on October 29, 2018.

Cresswell, P., Dirksen, G., Kley, W., & Nelson, R. P. 2007, A&A, 473, 329
 Dorn, C., Khan, A., Heng, K., et al. 2015, A&A, 577, 83
 Dressing, C. D. & Charbonneau, D. 2013, ApJ, 767, 95
 Espinoza, N., Brahm, R., Jordán, A., et al. 2016, ApJ, 830, 43
 Espinoza, N. & Jordán, A. 2016, MNRAS, 457, 3573
 Espinoza, N., Rackham, B. V., Jordán, A., et al. 2018, submitted to MNRAS (arXiv:1807.10652)
 Esteves, L. J., De Mooij, E. J. W., & Jayawardhana, R. 2015, ApJ, 804, 150
 Fabrycky, D. & Tremaine, S. 2007, ApJ, 669, 1298
 Foreman-Mackey, D., Hogg, D. W., Lang, D. & Goodman, J. 2013, PASP, 125, 306
 Foreman-Mackey, D., Agol, E., Ambikasaran, S. & Angus, R. 2017, AJ, 154, 220
 Fulton B. J., Petigura E. A. & Blunt S., Sinukoff E., 2018, PASP, 130, 986
 Gaia collaboration, Brown, A. G. A., Vallenari, A., et al. 2018, ArXiv e-prints, arXiv:1804.09365
 Gandolfi, D., Barragán, O., Livingston, J. H., et al. 2018, ArXiv e-prints, arXiv:1809.07573
 Gardner, J. P., Mather, J. C., Clampin, M., et al. 2006, Space Sci. Rev. 123, 485
 Guillot, T., & Showman, A. P. 2002, A&A, 385, 156
 Hartman, J. D., Bakos, G. Á., Torres, G., et al. 2011, ApJ, 742, 59
 Hartman, J. D., Bakos, G. Á., Bayliss, D., et al. 2018, AJ submitted, arXiv:1809.01048
 Heng, K., & Demory, B.-O. 2013, ApJ, 777, 100
 Huang, C. X., Burt, J., Vanderburg, A., et al. 2018, ArXiv e-prints, arXiv:1809.05967
 Kaltenegger, L. & Sasselov, D. 2011, ApJ, 736, L25
 Kaufer, A., Stahl, O., Tubbings, S. et al. 1999, The Messenger 95, 8
 Kreidberg, L. 2015, PASP, 127, 1161
 Kurucz, R. 1993, ATLAS9 Stellar Atmosphere Programs and 2 km/s grid. Kurucz CD-ROM No. 13. Cambridge, Mass.: Smithsonian Astrophysical Observatory, 1993.
 Jenkins, J. M., Twicken, J. D., McCauliff, S., et al. 2016, in Proc. SPIE, Vol. 9913, Software and Cyberinfrastructure for Astronomy IV, 99133E
 Jenkins, J. M. (ed.) 2017, Kepler Data Processing Handbook, KSCI-19081-002
 Jones, M. I., Jenkins, J. S., Rojo, P., & Melo, C. H. F. 2011, A&A, 536, A71
 Jones, M. I., Brahm, R., Wittenmyer, R. A., et al. 2017, A&A, 602, 58
 Jordán, A., Espinoza, N., Rabus, M., et al. 2013, ApJ, 778, 184
 Jordán, A., Brahm, R., Espinoza, N., et al. 2018, ArXiv e-prints, arXiv:1809.08879
 Madhusudhan, N., Amin, M. A. & Kennedy, G. M. 2014, ApJ, 794, L12
 Matsumura, S., Peale, S. J. & Rasio, F. A. 2010, ApJ, 725, 1995
 Mordasini, C., van Boekel, R., Molliere, P., et al. 2016, ApJ, 832, 41
 Mulders, G. D., Pascucci, I. & Apai, D. 2015, ApJ, 814, 130
 Paunzen, E. 2015, A&A, 580, A23
 Queloz, D., Eggenberger, A., Mayor, M., et al. 2000, A&A, 359, L13
 Queloz, D., Mayor, M., Udry, S., et al. 2001, The Messenger, 105, 1
 Rasio, F. A., Tout, C. A., Lubow, S. H. & Livio, M. 1996, ApJ, 470, 1187
 Ricker, G. R., Winn, J. N., Vanderspek, R., et al. 2015, Journal of Astronomical Telescope, Instruments and Systems, 1, 014003
 Schlegel, D. J., Finkbeiner, D. P., & Davis, M. 1998, ApJ, 500, 525

- Seager, S., & Sessalov, D. D. 2000, ApJ, 537, 916.
Sedaghati, E., Boffin, H. M. J., MacDonald, R. J., et al. 2017, Nature, 549, 238
Shporer, A. 2017, PASP, 129, 072001
Shporer, A., O'Rourke, J. G., Knutson, H. A., et al. 2014, ApJ, 788, 92
Sing, D. K., Fortney, J. J., Nikolov, N., et al. 2016, Nature, 529, 59
Snedden, C. 1973, ApJ, 184, 839
Snellen I. A. G., de Kok, R. J., le Poole R., Brogi M. & Birkby J. 2013, ApJ, 764, 182
Sousa, S. G., Santos, N. C., Adibekyan, V., Delgado-Mena, E., & Israelian, G. 2015, A&A, 577, A67
Stassun, K. G., Corsaro, E., Pepper, J. A., & Gaudi, B. S. 2018, AJ, 155, 22
Thorngren, D. P., Fortney, J. J.; Murray-Clay, R. A. & Lopez, E. D. 2016, ApJ, 831, 64
Tokovinin, A., Fischer, D. A., Bonati, M., et al. 2013, PASP, 125, 1336
Tokovinin, A. 2018, PASP, 130, 35002
Wang, S., Addison, B., Fischer, D. A., et al. 2018, AJ, 155, 70
Wang, S., Jones, M., Shporer, A., et al. 2018, ArXiv e-prints, arXiv:1810.02341
Weiss, L. M., Marcy, G. W., Rowe, J. F., et al. 2013, ApJ, 768, 14
Winn, J. N., Fabrycky, D., Albrecht, S., & Johnson, J. A. 2010, ApJ, 718, 145L
Winn, J. N. & Fabrycky, D. C. 2015, ARA&A, 53, 409
Yi, S., Demarque, P. Kim, Y.-C., et al. 2001, ApJS, 136, 417